

Scaling Training Data with Lossy Image Compression

Katherine L. Mentzer and Andrea Montanari*

July 26, 2024

Abstract

Empirically-determined scaling laws have been broadly successful in predicting the evolution of large machine learning models with training data and number of parameters. As a consequence, they have been useful for optimizing the allocation of limited resources, most notably compute time.

In certain applications, storage space is an important constraint, and data format needs to be chosen carefully as a consequence. Computer vision is a prominent example: images are inherently analog, but are always stored in a digital format using a finite number of bits. Given a dataset of digital images, the number of bits L to store each of them can be further reduced using lossy data compression. This, however, can degrade the quality of the model trained on such images, since each example has lower resolution.

In order to capture this trade-off and optimize storage of training data, we propose a ‘storage scaling law’ that describes the joint evolution of test error with sample size and *number of bits per image*. We prove that this law holds within a stylized model for image compression, and verify it empirically on two computer vision tasks, extracting the relevant parameters. We then show that this law can be used to optimize the lossy compression level. At given storage, models trained on optimally compressed images present a significantly smaller test error with respect to models trained on the original data. Finally, we investigate the potential benefits of randomizing the compression level.

1 Introduction

1.1 Background and motivation

Training in machine learning has reached a scale at which storage is becoming an important concern. The storage size of a recent published research datasets —LAION-5B [Schuhmann et al.(2022)]— is of the order of 100 TB, and this number is significantly larger in industry. Most companies in data-intensive domains (e.g. recommendation systems or autonomous vehicles) train models on petabyte scale data. Neural scaling laws [Kaplan et al.(2020), Hoffmann et al.(2022)] promise that any increase in the number of training samples will produce a predictable reduction¹ in the error rate thus providing a strong incentive towards accumulating increasingly massive datasets.

This trends suggest a natural question:

How should data scaling be extended under storage constraints?

Part of the answer is suggested by the observation that a significant fraction of these data is, at a fundamental level, analog (images, audio, video). Therefore, any digital format captures the original

*Granica

¹This of course holds under the condition that the model complexity is scaled simultaneously.

signal only with a finite degree of resolution. The resolution can be changed, therefore changing the required storage space. The ‘right’ level or resolution must ultimately be decided on the basis of a utility criterion.

Throughout this paper we will focus —to be definite— on the case of images and machine learning tasks in computer vision. Prevalent image formats, such as PNG or JPEG, target human perceptual metrics. These formats have lossy modes that allow to reduce the memory footprint at the cost of some image quality degradation. Nevertheless, the common practice is to use the highest available quality level or, at worst, to keep a format that is ‘visually lossless.’ This approach is not well justified and potentially wasteful, if data are used for machine learning training. Using more aggressive compression levels has the potential of addressing the storage constraint.

Several questions arise naturally:

1. How do models trained on (lossily) compressed images compare to models trained on uncompressed ones?
2. What is the optimal compression level to be used under a given storage constraint?
3. How does does lossy compression affect data scaling laws?

While there has been some work on these questions in the past [Dziugaite et al.(2016), Das et al.(2017), Yang et al.(2021), Dodge and Karam(2016)], even the most basic one is not settled. In this paper we instead hypothesize a complete picture and show that it can be used to push data scaling in a more efficient way.

1.2 Summary of results

We contend that, when storage is an important constraint, we should think about scaling laws not in terms of number of samples but (also) in terms of bits. Our main finding is that machine learning generalization can be described, in a suitable storage-limited regime, by a bits-samples scaling law.

Consider a setting in which we are given n training samples $\{\mathbf{z}_i\}_{i \leq n}$. To be definite, in an image classification task, $\mathbf{z}_i = (\mathbf{x}_i, y_i)$, where \mathbf{x}_i is an image and y_i is the corresponding label (for a K -classes task, $y_i \in \{1, \dots, K\}$). We think of $\mathbf{z}_i = (\mathbf{x}_i, y_i)$ as an object potentially requiring infinitely many bits to be specified. For instance \mathbf{x}_i could be an analog grayscale image (modeled as a function $\mathbf{x}_i : [0, 1]^2 \rightarrow \mathbb{R}$).

We train a machine learning model using an L -bits representation of the above samples, denoted by $\mathbf{z}_i(L)$. For instance, in the case of images, we could use JPEG or JXL lossy modes to obtain L -bits representations. Letting $\hat{f}(\cdot; n, L)$ denote the model trained on such L -bits images, we denote by $\text{Err}_{\text{test}}(n, L)$ be the test error on original (uncompressed images):

$$\text{Err}_{\text{test}}(n, L) = \mathbb{E} \Delta(y_i, f(\mathbf{x}_i; n, L)). \quad (1)$$

Here $\Delta(y, \hat{y})$ is a suitable loss function for the task of interest. For instance this could be classification loss $\Delta(y, \hat{y}) = 1$ if $\hat{y} \neq y$ and $\Delta(y, \hat{y}) = 0$ if $\hat{y} = y$.

We hypothesize that, in a suitable regime of n, L , the test error is well approximated by the following scaling law

$$\text{Err}_{\text{test}}(n, L) \approx \text{Err}_{\text{test}}^* + A \cdot n^{-\alpha} + B \cdot L^{-\beta}, \quad (2)$$

for some constants $\text{Err}_{\text{test}}^*$, A , B and scaling exponents $\alpha, \beta > 0$. It is important to emphasize that these parameters will depend on the specific setting. Namely, they might depend on the machine

learning task, on the dataset, on the model, on the compression algorithm, and so on. In particular, $\text{Err}_{\text{test}}^*$ should not be interpreted as the Bayes error, but only as the minimal error attainable by the model under consideration. We discuss these and other limitations and generalizations of Eq. (2) in Section 4.

When verified, Eq. (2) provides a principled way to choose the level of compression for training data, by solving storage-constrained optimization problem (here, we denote by s the total available storage):

$$\begin{aligned} & \text{minimize} && A \cdot n^{-\alpha} + B \cdot L^{-\beta}, \\ & \text{subj. to} && n \cdot L = s. \end{aligned} \tag{3}$$

This yields the optimal solution $L_*(s) = Cs^{\alpha/(\alpha+\beta)}$, $n_*(s) = C^{-1}s^{\beta/(\alpha+\beta)}$, with $C = (\beta B/\alpha A)^{1/(\alpha+\beta)}$ with corresponding test error

$$\text{Err}_{\text{test}}(n_*(s), L_*(s)) \approx \text{Err}_{\text{test}}^* + C_E \cdot s^{-\nu}, \quad \nu = \frac{\alpha\beta}{\alpha + \beta}, \tag{4}$$

for a constant C_E . Interestingly, the resulting storage scaling exponent is not given by either the sample size exponent α nor by the bits exponent β , but by their harmonic mean.

The rest of this paper is devoted to providing evidence for the scaling law (2) and its utility in optimally scaling the sample size n and the bits per samples L (hence the compression level):

1. In Section 2 we present results of numerical experiments on three computer vision tasks: image classification, semantic segmentation, and object detection. We verify that the test error is well described by the scaling law (2), and that optimizing the predicted tradeoff between bits and samples yields near-optimal scaling of test error with storage.²
2. In Section 3, we propose a very simple stylized model for image compression. We prove that the scaling law (2) naturally arise as a consequence of the multiresolution structure of natural images.

Finally, we discuss limitations and extensions of the present approach in Section 4.

1.3 Related Work

Scaling laws have proven a useful tool to capture the evolution of the test error with model complexity and number of training samples. In their most successful version [Hestness et al.(2017), Rosenfeld et al.(2019)], they describe the dependence of Err_{test} on the number of training samples n , and the number of model parameters m , while keeping fixed the model architecture, and the specifics of the training algorithm. A scaling law postulates a power-law dependence on these two resources: $\text{Err}_{\text{test}}(n, m) \approx a \cdot n^{-\alpha} + b \cdot m^{-\gamma}$. In this paper, we follow the same line of work and propose to treat the number of bits per sample as the relevant resource (in addition to the number of samples), in the storage-limited regime.

Motivated by the practical utility of scaling laws, a number of authors have studied generalizations to incorporate the dependence on computational resources [Henighan et al.(2020), Kaplan et al.(2020), Bahri et al.(2021), Alabdulmohsin et al.(2022)], their applicability to finetuning a model that has been pretrained on a large dataset [Hernandez et al.(2021), Tay et al.(2021)], their extrapolation properties [Hoffmann et al.(2022)], and the impact of data repetition in the data-constrained regime [Muennighoff et al.(2023)]. Such laws have found their most important application in the allocation of resource to data scaling versus compute scaling.

²The code is available at <https://github.com/granica-ai/LossyCompressionScalingKDD2024>.

In practice, images are stored using a number of different codecs, with JPEG [?] and PNG [?] among the most popular lossy and lossless methods, respectively. More modern codecs, such as JPEG XL [Alakuijala et al.(2019)], take advantage of human perception to achieve higher compression levels for approximately the same amount of visual or perceptual change to the image. Neural image compression is also an active area of research, with findings indicating that the human perception of an image can be largely preserved with many fewer bits [Rombach et al.(2022), Theis et al.(2022)].

Lossy compression of training images is implicit in the widespread use of JPEG. However, the consequences of compression and image resolution/loss on the resulting models are poorly understood, and the commonly accepted practice is to store training images at the highest available resolutions (‘lossless’ or ‘visually lossless’). Nonetheless, when images are lossily compressed, the impact on training is not well understood. Several studies suggest that lossy image compression may help computer vision models by removing distracting noise or reducing adversarial perturbations [Dziugaite et al.(2016), Das et al.(2017), Yang et al.(2021)]. Other studies point out that lossy compression also discards information in the image, reducing image quality and sometimes leading to less accurate predictions [Dodge and Karam(2016)].

2 Empirical Results

2.1 Set up

In this section, we investigate the impact of scaling training data storage for three computer vision tasks: (1) An image classification task using the multi-class Food101 dataset [Bossard et al.(2014)] and a ResNet50 architecture [He et al.(2016)] pretrained on ImageNet-1K [Vryniotis(2021)]; (2) a semantic segmentation task using the Cityscapes dataset [Cordts et al.(2016)] and a b5 SegFormer architecture [Xie et al.(2021)], also pretrained on ImageNet-1K; (3) a object detection task on aerial images using the iSAID dataset [Waqas Zamir et al.(2019)] and a a Mask R-CNN architecture [He et al.(2017)].

As anticipated in the introduction, we are interested in the dependence of test error on n (the number of of training images) and L (which we redefine here as number of bytes per image). We achieve different values of n by selecting subsets of the training data. We achieve different values of L by using different levels of JPEG XL (JXL) lossy image compression [Alakuijala et al.(2019)]. Note that a fixed byte size is difficult to achieve, so we use L do denote the average byte size instead.

The JXL compression level is determined by a perceptual distance metric, Butteraugli distance, with a higher distance corresponding to stronger compression and lower image quality. We train models on a grid of n and L values. Test error, Err_{test} , is measured in percent of images incorrectly classified for the classification task and one minus the mean intersection over union (mIoU) metric for the semantic segmentation task. For the object detection task, we select the bounding box mean average precision on small objects (less than 32^2 pixels)—this metric is one of the standard COCO evaluation metrics [Lin et al.(2014)], and we select it to explore the impact of compression on smaller features in images.

For each set of data gathered in this way, we fit the scaling law (2) to the measured test error, to extract parameters $\text{Err}_{\text{test}}^*$, A , B , and exponents α , β .

2.2 Scaling curves

For each task, we select n and L values in the following way. The n values for each dataset are approximately 20%, 40%, 60%, 80%, and 100% of a train split for each dataset. In the case

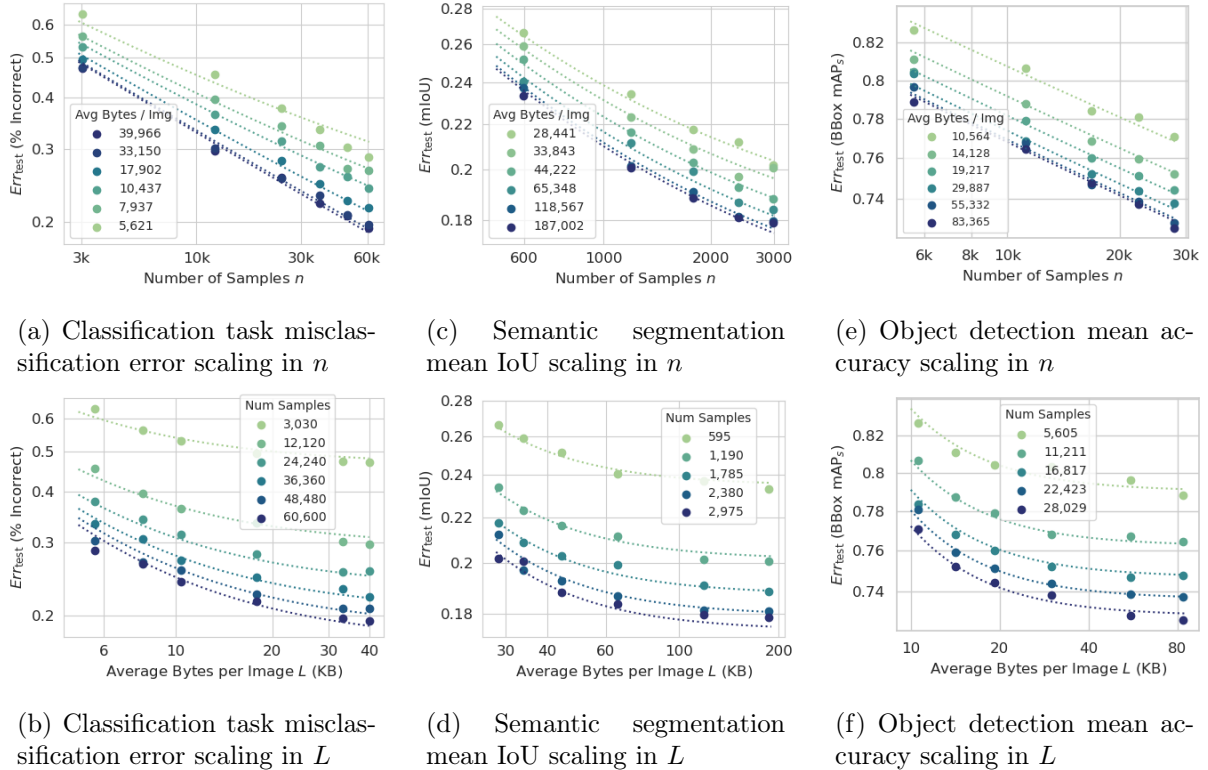


Figure 1: Test error scaling for the image classification, semantic segmentation, and object detection tasks. Circles represent empirical results, and the dotted line indicates the scaling curve fit to these observations.

of the image classification task, these samples are stratified, maintaining class balance in each subset. The range of n values varies significantly between tasks due to the differing sizes of the datasets. To achieve different L values, we compress images using JXL to Butteraugli distances $Bd \in \{1, 2, 4, 7, 10, 15\}$, where higher distances correspond to smaller average byte sizes L . Training procedures mimic the training method for each model’s original paper, and the approaches are detailed in Appendix A.

Figure 1 shows the resulting scaling curves for the three computer vision tasks. Circles indicate empirical model test errors, and the dotted line illustrates curve that we fit to these average test errors. Table 1 shows the parameters for these fit curves.

Task	A	B	Err_{test}^*	α	β
Classification	6.7	1.4×10^3	0.0	0.33	1.06
Segmentation	4.3	4.3×10^5	0.1	0.59	1.6
Detection	1.0	2.7×10^5	0.3	0.09	1.7

Table 1: Scaling curve fit parameters for each task, where curves take the form $Err_{\text{test}}(n, L) \approx Err_{\text{test}}^* + A \cdot n^{-\alpha} + B \cdot L^{-\beta}$.

We observe that the test error decreases with n and L as expected, and that this behavior is well approximated by the scaling law (2). We note that while the plots are shown with log-scale axes, the curves are not precisely linear. This is a consequence of the fact that the scaling law (2)

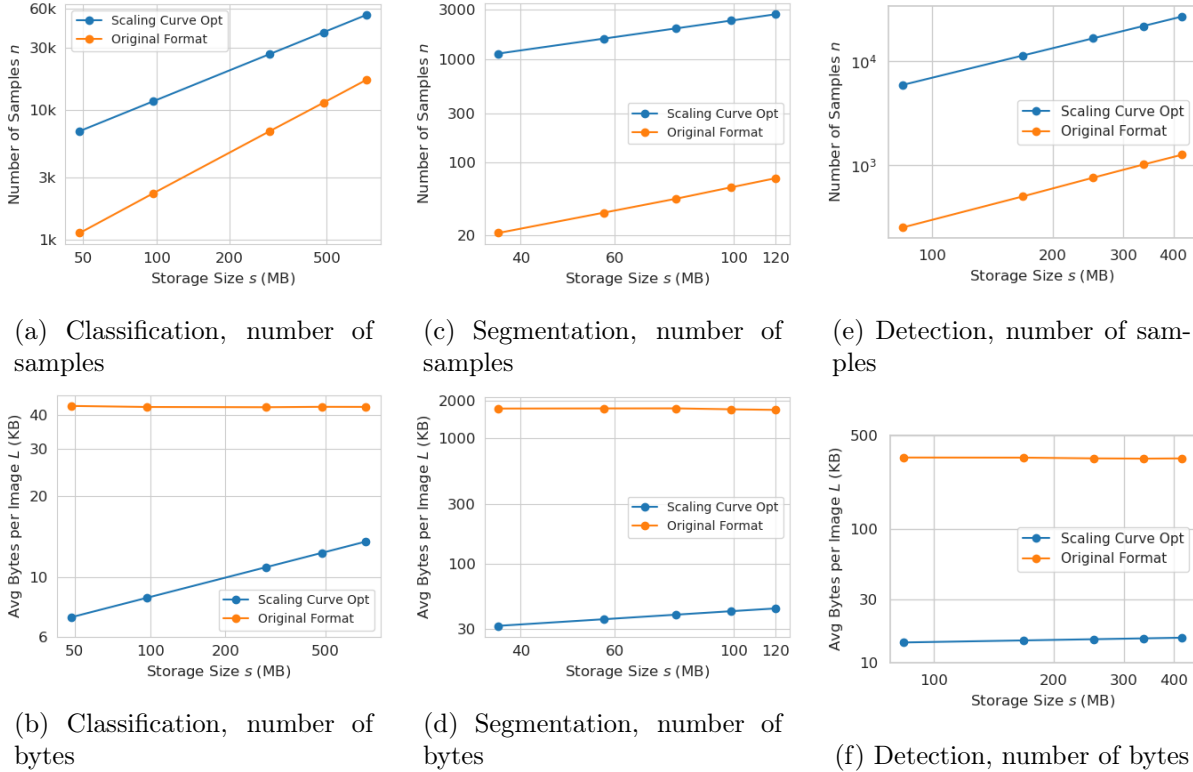


Figure 2: Values of n and L as a function of total storage size for each task under the optimal and original format training data.

is the sum of contributions. If we vary only n or only L , the excess error $\text{Err}_{\text{test}}(n, L) - \text{Err}_{\text{test}}^*$ will saturate at a strictly positive level. We also observe that the exponent β is typically larger than α , indicating that the effect of short-scale details decays rather rapidly. However, the last conclusion is likely to be sensitive to the specific task under study. Furthermore, this power law pattern is not unique to these chosen metrics; we find other measures of error follow similar patterns, shown in [Appendix B](#).

2.3 Optimizing n and L

Given a scaling law that fits the data, and a fixed storage value s , we can determine the optimal $n_*(s)$ and $L_*(s)$ to minimize the predicted test error, as per Eq. (3). The behavior $n_*(s)$ and $L_*(s)$ according to our model suggests that, in the storage-limited regime, opting for more images of lower quality can improve model performance over fewer, less compressed images.

Figure 2 illustrates the optimal $n_*(s)$ and $L_*(s)$ values under our model for each task. We compare number of images at a given storage level s to the number of images in original format (i.e. without lossy compression) that fit into the given storage. The curves for the image classification task in Figure 2a-b illustrate that leaving images in their original JPEG format results in a larger higher L and lower n than optimal, if the goal is to minimize test error. If the images are previously stored as PNGs, as in the semantic segmentation task and the object detection tasks, this effect is even more pronounced, as illustrated in Figure 2c-d and Figure 2e-f. Table 2 also captures these results. Hence, giving up some image quality (via lossy compression) to acquire a greater number of example images is preferable in this storage-limited setting.

Classification Task			Segmentation Task			Detection Task		
s	$n_*(s)$	$L_*(s)$	s	$n_*(s)$	$L_*(s)$	s	$n_*(s)$	$L_*(s)$
48,480,000	6,838	7,087	36,360,000	1,137	31,965	84,087,000	5,913	14,219
96,960,000	11,588	8,363	57,267,000	1,586	36,090	168,174,000	11,417	14,730
290,880,000	26,737	10,876	78,174,000	1,991	39,254	252,261,000	16,776	15,037
484,800,000	39,441	12,289	99,080,999	2,368	41,831	336,348,000	22,043	15,258
727,200,000	53,697	13,540	119,988,000	2,725	44,016	420,435,000	27,243	15,433

Table 2: Optimal n and L for the classification, segmentation, and detection tasks, according to the fit scaling curves. L is the average bytes per pixel; that is, the empirical dataset size in bytes divided by the number of images in the subset.

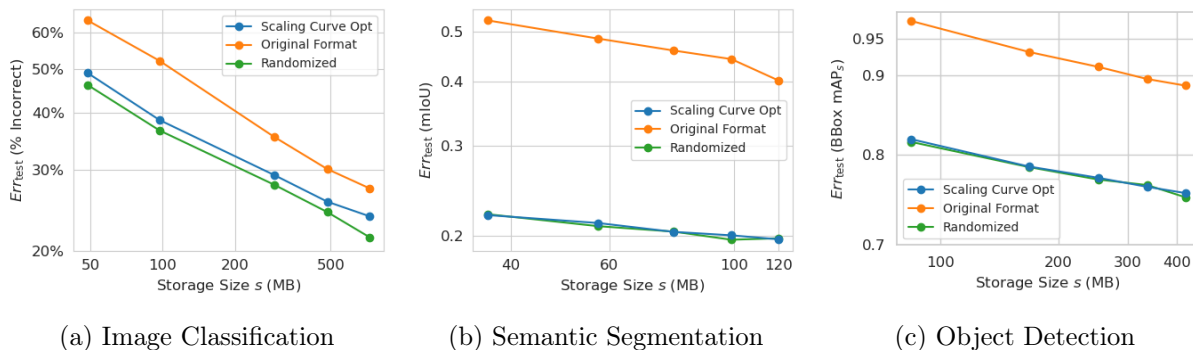


Figure 3: Test error scaling in s for each task using different data scaling schemes.

2.4 Test error for optimal n and L

The scaling curves suggest that the optimal trade-off between n and L requires more compression than used in standard image storage formats. We next explore the impact of optimizing this tradeoff on test error. Namely, we consider the following storage sizes $s \in [4848, 9696, 29088, 48480, 72720] \times 10^4$ (for classification) $s \in [3636, 5726.7, 7817.4, 9908.1, 11998.8] \times 10^4$ (for segmentation), and $s \in [8408.7, 16817.4, 25226.1, 33634.8, 42043.5] \times 10^4$ (for detection) and train models using the following data scaling schemes.

Scaling Optimal. For each s calculate the optimal $n_*(s)$ and $L_*(s)$ that minimize the test error according to the fitted scaling law. We then select stratified subsets of the dataset of size $n_*(s)$ and search for the image compression level that achieves the target $L_*(s)$ on average. Note that all images are compressed using the same compression parameters, but the bytes per image may vary between images based on image content and compression characteristics. We train a model using the same architecture and hyperparameters as the scaling curve models. To average over the effect of the specific subset selected for each model, we repeat this process 2 more times for a total of 3 models trained at each $n_*(s)$ and $L_*(s)$ value. We report accuracy averaged over these 3 iterations.

Original Format. An alternative to allowing lossy compression is to retain full image resolution; to achieve the desired storage capacity, we simply discard images until the training images fit within the budgeted space. For each storage size s used in the scaling optimal models, we train a model based on an original format subset that occupies the same amount of storage. The JXL image

codec typically outperforms older image codecs such as PNG and JPEG; therefore, for a most fair comparison to the lossily compressed JXL images, we use the JXL version of the original data storage to calculate the storage size of a given subset—i.e., the Food101 data, originally stored as JPEGs, is compressed using the JPEG to JXL transcoding that does not introduce further loss, and the Cityscapes and iSAID datasets, originally stored as PNGs, are compressed using JXL lossless mode. In a slight abuse of notation, we still refer to these JXL versions that do not introduce further loss as ‘original format.’ Under this encoding, the average bytes per pixel is $L = 42,804$ for the Food101 dataset, $L = 1,711,011$ for the Cityscapes dataset, and $L = 337,789$ for the iSAID dataset. The resulting subsets are then used to train a model with the same parameters as the original scaling curves.

Randomized. The scaling optimal models use the optimal $n_*(s)$ and $L_*(s)$ for a given fixed storage, where all images are compressed to the same level. We investigate the effect of heterogeneity in the compression levels. One might argue that heterogeneous compression can lead to models benefiting from exposure to both more and less compressed images.

Our randomization strategy is as follows. Using the same image subsets as the scaling optimal training images, we compress each image to some level within a range of different compression levels. To generate the range of compression levels, the training images are randomly ordered. This ordering is then translated into a compression level, where the first ranked image is compressed to the lowest level, the last ranked image is compressed to the highest level, and the remaining images are uniformly spaced in between. To determine the minimum and maximum compression level, we use the following procedure. The minimum compression level is the smallest non-negative JXL distance that leads to compression relative to the original storage format — in practice, a distance of 0.5 for the Food101 dataset and 0 for the Cityscapes and iSAID datasets. The maximum compression level is then increased until the subset reaches the desired compressed size or a distance of 15. If a distance of 15 is reached and the subset is still too large with regard to compressed size, the minimum compression level is increased until the images reach the desired compressed size. We selected the maximum distance of 15 due to diminishing reductions in file size beyond this distance. Once we find a mapping of images to compression levels that achieves the target storage size, we then train a model using the same parameters as the original scaling curves.

Figure 3a shows the test error of each of these strategies for the image classification task, averaged over three different realizations of model training. The original format models performs significantly worse than the scaling optimal models. Furthermore, the randomized curve shows a small but consistent benefit over the uniformly compressed scaling curve optimal result, suggesting that this model indeed benefits from exposure to a variety of compression levels.

Figure 3b shows the same results for the segmentation task. Due to the Cityscapes images original PNG format, the number of losslessly compressed images that fit into the storage budget is very low (fewer than 100 samples). Consequently, models trained on so few images perform significantly worse than models trained on more, lossily-compressed images. Furthermore, the randomized results are noisier, with variable results compared to the uniformly compressed scaling curve optimal models. The object detection results, shown in Figure 3c, follow a similar structure, as the original image format was also PNG.

2.5 Comparison to naive compression

We next explore the benefits of using scaling optimal compression over fixed-level compression. Figure 4 compares the test error at the optimal values of n and L to the test error for other (fixed) compression levels. Similar to the original format curve in Figures 3a and 3b, we select the greatest

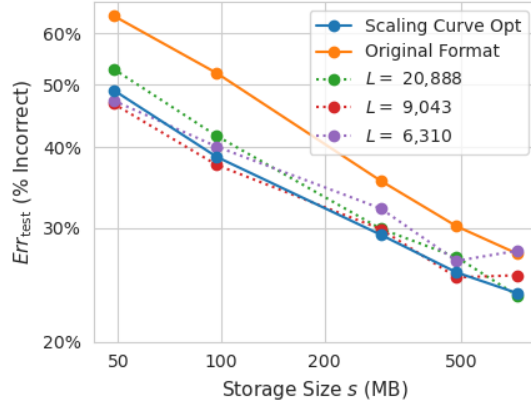


Figure 4: Test error for models trained on naively compressed data relative to test error for models trained on optimally compressed data and original format data.

number of images that fit within the storage budget at the given level of compression. For each value of s , we generate 3 different data subsets and train 3 models, reporting the average test error. To reduce the variability due to the specific data subset, the subsets are chosen to overlap as much as possible with the subsets used to train the 3 models that comprise the optimal curve.

We observe that fixed compression levels typically lead to the same or higher test error than the optimally selected value $L_*(s)$, though they have an advantage over original format data. At the smallest storage sizes, results are more variable—test error varies based on the specific subset of images used to train the model, leading to a less clear benefit from compression level optimization. For example, at the lowest storage levels, the $L = 6,310$ and $L = 9,043$ models perform slightly better than the optimal $L = 6,838$ model, despite the naive models landing on opposite sides of the n versus L trade-off relative to the optimal. This result can be attributed to the higher variability of model performance at lower storage sizes and the differences in the specific examples used for training.

2.6 Test set compression

The scaling law (2) predicts how models trained on differently compressed data performs on uncompressed test data. A natural question is how these models perform on compressed test sets. To investigate this question, we take the largest n model trained at each compression level L and evaluate it on a number of compressed test sets. The scaling models were trained on JXL images compressed to Butteraugli distances $Bd \in \{1, 2, 4, 7, 10, 15\}$, and we evaluate each model on a test set compressed to these same Butteraugli distances. The result is 6 different test accuracy results for each of 6 different models.

The circles in Figure 5 represent these accuracies, and the background color is a linear interpolation of these observations. Unsurprisingly, the highest test accuracy is typically when the model is evaluated on data that is compressed to the same level as the training data (i.e., when the test and train data is most similar). More interestingly, for all three tasks, the largest reduction in performance is for models trained on low compression levels but evaluated on highly compressed data. Models trained on somewhat more compressed data see less performance degradation, demonstrating some robustness to variability in test data quality.

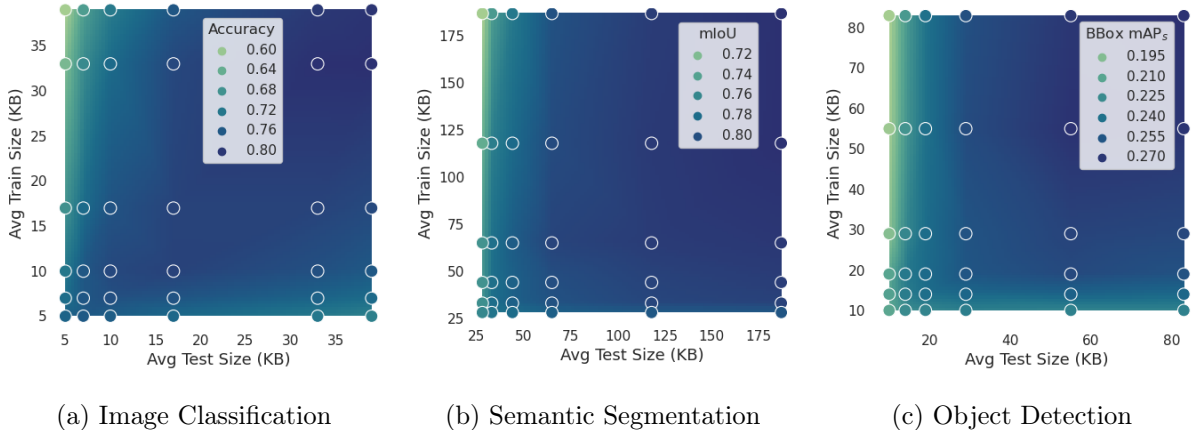


Figure 5: Error as a function of both training data compression level and test data compression level for the classification, segmentation, and detection tasks. Circles indicate empirical results from model evaluation, and the background represents a linear interpolation of those points.

3 A stylized model

In this section we introduce a stylized model for machine learning from compressed images. To motivate this model, consider the case of a grayscale image, modeled as a function $f : [0, 1]^2 \rightarrow \mathbb{R}$. For image processing purposes, this is most conveniently represented in a multiscale fashion [Daubechies(1992), Mallat(1999)], e.g. via wavelet transform. Schematically, for $\mathbf{r} \in [0, 1]^2$

$$f(\mathbf{r}) = \sum_{\ell=0}^{\infty} \sum_{\mathbf{k} \in [q_0^\ell]^2} x_{\mathbf{k}}^{(\ell)} \psi(q_0^\ell(\mathbf{r} - \mathbf{k}q_0^{-\ell})). \quad (5)$$

Here ψ is the basis wavelet and $\{x_{\mathbf{k}}^{(\ell)} : \mathbf{k} \in [q_0^\ell]^2\}$ are $q_0^{2\ell}$ coefficients at scale ℓ .

Part of the motivation for considering this representation stems from the fact that standard lossy compression schemes (such as JPEG or JXL) are fundamentally based on multiscale analysis, albeit in a simplified form [Donoho et al.(1998)]. To a first order, lossy compression is achieved by quantizing to a coarser level (or completely setting to zero) smaller scale coefficients.

Rather than noting explicitly \mathbf{k} as a two-dimensional index, we will directly think an example as an infinite vector

$$\mathbf{x} = (\mathbf{x}^{(0)}, \mathbf{x}^{(1)}, \mathbf{x}^{(2)}, \dots), \quad \mathbf{x}^{(\ell)} \in \mathbb{R}^{q^\ell}, \quad (6)$$

with $\mathbf{x}^{(\ell)} = (x_1^{(\ell)}, \dots, x_{q^\ell}^{(\ell)})$. To make a connection with the image setting, we can choose $q = q_0^2$. As a cartoon for a lossy compression algorithm, we consider the scheme that truncates the multiscale coefficients at level m

$$\Phi_m(\mathbf{x}) = (\mathbf{x}^{(0)}, \mathbf{x}^{(1)}, \mathbf{x}^{(2)}, \dots, \mathbf{x}^{(m)}), \quad L = \sum_{\ell=0}^m q^\ell. \quad (7)$$

We identify L as the number of bits in our compressed representation. This does not change scaling laws, as long as each coordinate of \mathbf{x} can be represented by a constant (independent of n, L) number of bits (one byte is common in image formats).

We consider the simplest model of supervised learning. We are given samples $(y_i, \mathbf{x}_i) \in \mathbb{R} \times \mathbb{R}^\infty$, $i \leq n$, whereby

$$y_i = \langle \mathbf{x}_i, \boldsymbol{\theta} \rangle + \varepsilon_i, \quad \mathbb{E}(\varepsilon_i^2) = \tau^2, \quad (8)$$

where the noise variables ε_i have zero mean and are i.i.d. and independent of everything else. Given such a model, it is natural to estimate the coefficients $\boldsymbol{\theta} \in \mathbb{R}^\infty$ via ridge regression. This classical approach has recently drawn renewed interest because of its mathematical equivalence to kernel ridge regression, and its connection to neural networks in the linear regime.

Since we want to perform learning on compressed data, we use the vectors $\Phi_m(\mathbf{x}_i)$ in learning:

$$\hat{\boldsymbol{\theta}}_\lambda(n, L) = \arg \min_{\mathbf{b} \in \mathbb{R}^L} \left\{ \sum_{i=1}^n (y_i - \langle \mathbf{b}, \Phi_m(\mathbf{x}_i) \rangle)^2 + \lambda \|\mathbf{b}\|^2 \right\}. \quad (9)$$

We square loss also to define test error, namely

$$\text{Err}_{\text{test}}(n, L) = \mathbb{E} \left\{ \left(y_{\text{test}} - \langle \hat{\boldsymbol{\theta}}_\lambda(n, L), \Phi_m(\mathbf{x}_{\text{test}}) \rangle \right)^2 \right\}, \quad (10)$$

where $(y_{\text{test}}, \mathbf{x}_{\text{test}})$ is a fresh sample distributed as the training data $\{(y_i, \mathbf{x}_i)\}_{i \leq n}$.

It is a well-documented empirical observation that small scale components of natural images carry less energy than large scale components. Further, energy typically decays as a power law of the length scale. Since the length scale for block ℓ is $q_0^{-\ell}$, this translates into an exponential decay with ℓ . We assume a simple model that captures this behavior, namely the blocks $\mathbf{x}^{(\ell)}$, $\ell \geq 0$ are mutually independent with $\mathbb{E}\{\mathbf{x}^{(\ell)}\} = \mathbf{0}$ and

$$\mathbb{E}\{\mathbf{x}^{(\ell)}(\mathbf{x}^{(\ell)})^\top\} = s_\ell \mathbf{I}_{q^\ell}, \quad K_1 p^{-\ell} \leq s_\ell \leq K_2 p^{-\ell}, \quad (11)$$

where $p > 1$ is a model parameter and $0 < K_1 < K_2$ are constants. We will further assume the distribution of $\mathbf{x}^{(\ell)}$ to satisfy some technical conditions stated in Assumption 1, see Appendix C. Note that the expected total energy is $\mathbb{E}\|\mathbf{x}\|^2 \asymp \sum_{\ell \geq 0} (q/p)^\ell$: in order for this to be finite, we require $q < p$.

Finally, it is natural to assume that smaller scale component will have decreasing importance for our supervised learning task. We model this by writing the multiscale decomposition of the parameters $\boldsymbol{\theta}$ as $\boldsymbol{\theta} = (\boldsymbol{\theta}^{(0)}, \boldsymbol{\theta}^{(1)}, \boldsymbol{\theta}^{(2)}, \dots)$, and assuming, for some $r < 1$ and constants $0 < \tilde{K}_1 < \tilde{K}_2$:

$$\tilde{K}_1 r^\ell \leq \|\boldsymbol{\theta}^{(\ell)}\|^2 \leq \tilde{K}_2 r^\ell. \quad (12)$$

Under this model, the test error the test error (10) can be rewritten as

$$\begin{aligned} \text{Err}_{\text{test}}(n, L) &= \\ &= \tau^2 + \sum_{\ell=0}^m \mathbb{E}\{\langle \hat{\boldsymbol{\theta}}^{(\ell)} - \boldsymbol{\theta}^{(\ell)}, \mathbf{x}^{(\ell)} \rangle^2\} + \sum_{\ell=m+1}^{\infty} \mathbb{E}\{\langle \boldsymbol{\theta}^{(\ell)}, \mathbf{x}^{(\ell)} \rangle^2\} \\ &= \tau^2 + \sum_{\ell=0}^m \mathbb{E}\{\langle \hat{\boldsymbol{\theta}}^{(\ell)} - \boldsymbol{\theta}^{(\ell)}, \mathbf{x}^{(\ell)} \rangle^2\} + \bar{K}_m \cdot (r/p)^m, \end{aligned} \quad (13)$$

where $K_1 \tilde{K}_1 r / (p-r) \leq \bar{K}_m \leq K_2 \tilde{K}_2 r / (p-r)$. This expression corresponds to the decomposition of the test error in three terms, reflecting the scaling form (2): a fundamental limit τ^2 (in the present case, this is just the Bayes error); an statistical estimation error, corresponding to the sum over $\ell \leq m$; and a compression-induced error, corresponding to the smaller length scales, i.e. $\ell > m$.

The next result shows that indeed this decomposition reproduces the scaling law (2).

Theorem 1. *Under the model described above, further assume $rp < 1$, $q/p < 1$ and the conditions of Assumption 1 to hold. Then there exist positive constants $0 < A_1 < A_2$, $0 < B_1 < B_2$, $0 < C$, $0 < c_0$ (depending on the constants p, q, r, τ in the assumptions), such that, for all $n \leq c_* L^{1+2\kappa}$, and $\lambda \in [1/M, M] \cdot n^{(\kappa+1)/(2\kappa+1)}$ for some constant M ($\kappa := \log p / \log q$), the following holds with high probability*

$$\tau^2 + A_1 \cdot n^{-\alpha} + B_2 L^{-\beta} \leq \mathbb{E}_\varepsilon \text{Err}_{\text{test}}(n, L) \leq \tau^2 + A_2 \cdot n^{-\alpha} + B_2 L^{-\beta},$$

with exponents

$$\alpha = \frac{2 \log p}{2 \log p + \log q}, \quad \beta = \frac{\log(p/r)}{\log q}. \quad (14)$$

(In the above formulas, \mathbb{E}_ε denotes expectation with respect to the noise in the observations $\varepsilon_1, \dots, \varepsilon_n$.)

The proof of this result is given in Appendix C, and builds upon recent characterizations of high-dimensional ridge regression [Cheng and Montanari(2022), Tsigler and Bartlett(2023)]. We note that the same proof can be used also to characterize the behavior $n > c_0 L$. For the sake of brevity, we omit to state that result here.

In fact our analysis provides a sharper (albeit more complicated) characterization of test error than what stated in Theorem 1. In order to state this characterization, we introduce the following functions from [Cheng and Montanari(2022)]. First, define λ_* as the unique non-negative solution of

$$n - \frac{\lambda}{\lambda_*} = \sum_{\ell=0}^m \frac{s_\ell q^\ell}{s_\ell + \lambda_*}. \quad (15)$$

We then define

$$\mathbb{B}(m, n) := \frac{n \lambda_*^2}{n - \mathbb{D}(m)} \sum_{\ell=0}^m \frac{s_\ell \|\boldsymbol{\theta}^{(\ell)}\|^2}{(s_\ell + \lambda_*)^2}, \quad (16)$$

$$\mathbb{V}(m, n) := \frac{\mathbb{D}(m)}{n - \mathbb{D}(m)}, \quad (17)$$

where

$$\mathbb{D}(m) = \sum_{\ell=0}^m \frac{s_\ell^2 q^\ell}{(s_\ell + \lambda_*)^2}. \quad (18)$$

Lemma 1. *Under the assumptions of Theorem 1, consider $\lambda \geq n^{1-\kappa}/M$ for any constant M . Then we have*

$$\mathbb{E}_\varepsilon \text{Err}_{\text{test}}(n, L) = \tau^2 + \mathcal{B}(m, n) + \tilde{\tau}_m^2 \mathcal{V}(m, n) + \bar{K}_m \cdot (r/p)^m.$$

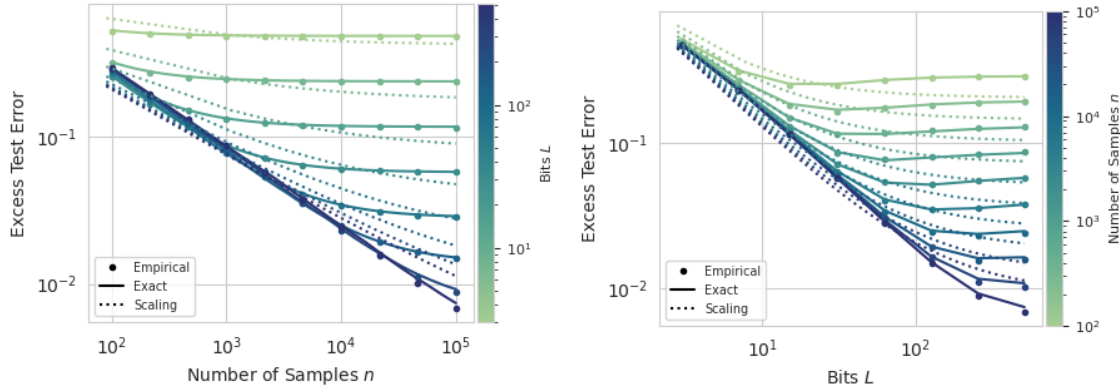
where (as above) $K_1 \tilde{K}_1 r / (p - r) \leq \bar{K}_m \leq K_2 \tilde{K}_2 r / (p - r)$,

$$\tilde{\tau}_m^2 = \tau^2 + \bar{K}_m \cdot (r/p)^m, \quad (19)$$

and

$$\mathcal{B}(m, n) = (1 + O(n^{-0.49})) \mathbb{B}(m, n), \quad (20)$$

$$\mathcal{V}(m, n) = (1 + O(n^{-0.99})) \mathbb{V}(m, n). \quad (21)$$



(a) Excess test error scaling in n for the stylized model.

(b) Excess test error scaling in L for the stylized model.

Figure 6: Simulation results of the stylized model indicate similar scaling patterns to the empirical data. Dots indicate the empirical simulation results, the solid line indicates the exact model described in Lemma 1, and the dotted line indicates the scaling curve fit to the empirical results.

As shown via simulation in Fig. 6, the model introduced in this section can indeed present behaviors similar to the empirical scaling law observed in section 2. In this small simulation, image vectors are drawn with each component $x_i^{(\ell)}$ uniform in $[-\sqrt{3p^{-\ell}}, \sqrt{3p^{-\ell}}]$ for $\ell \in \{1, \dots, m\}$ and $i \in \{1, \dots, p^\ell\}$ (hence choosing $x^{(\ell)}$ such that $\mathbb{E}\{\mathbf{x}^{(\ell)}(\mathbf{x}^{(\ell)})^\top\} = p^{-\ell} \mathbf{I}_{q^\ell}$). We let $\boldsymbol{\theta}^{(\ell)} = \mathbf{1} \cdot \sqrt{r^\ell q^{-\ell}}$ for $\ell \in \{1, \dots, m\}$, where $\mathbf{1}$ is the all ones vector of length q^ℓ (hence $\boldsymbol{\theta}^{(\ell)}$ is such that $\|\boldsymbol{\theta}^{(\ell)}\|^2 = r^\ell$). We use the parameters $q = 2$, $p = 2.1$, $r = 0.99$, and $\tau = 1$ and optimize over the ridge regression regularization parameter. The empirical results, represented as circles, align closely with the curves dictated by Lemma 1, represented as the solid lines. The dotted line represents the scaling law curve that is fit to the empirical data points. The fitted exponents in this synthetic example, $\alpha = 0.45$ and $\beta = 1.02$, are similar to the classification task, and are relatively close to the exponents prescribed by Theorem 1 ($\alpha = 0.67$ and $\beta = 1.02$).

4 Discussion

The scaling law studied in this paper admits some natural generalization. The most obvious limitation is that we consider the model complexity as fixed, and therefore $\text{Err}_{\text{test}}^*$ represents the minimum test error achievable by the model under consideration on a given task. If we vary the model complexity, as measured for instance by the number of parameters m , this quantity will change. The common hypothesis in that case [Hestness et al.(2017), Kaplan et al.(2020)] is that $\text{Err}_{\text{test}}^*(m) \approx \text{Err}_{\text{Bayes}} + C \cdot m^{-\gamma}$, where $\text{Err}_{\text{Bayes}}$ is the Bayes error, and C, γ are parameters. This suggests to generalize the scaling law (2) as

$$\text{Err}_{\text{test}}(n, L) \approx \text{Err}_{\text{Bayes}} + A \cdot n^{-\alpha} + B \cdot L^{-\beta} + C \cdot m^{-\gamma}. \quad (22)$$

It would be interesting to test this extended law in future work.

We expect the coefficients A, B and exponents α, β to depend on the task under consideration. For instance, in medical image classification [Cai et al.(2020)], we are often interested in detecting small patterns in a high-resolution image. In this case, the dependence on short scale components, and hence the number of bits L will be stronger. We see evidence of this pattern in the aerial image

object detection task here, where the small object test error has a scaling pattern with β an order of magnitude larger than α . It would be important to develop some understand of this variability, as much as the limits of validity of Eq. (2).

Moreover, the randomized strategy explored in this work provides evidence that more nuanced compression strategies may yield better results than uniformly compressing each image using the same compression settings. Additional methods of mapping images to compression levels may improve results further.

Finally, the main recommendation that emerges from this work is both simple and practical: The “default” approach of leaving images in lossless full resolution results in too high L and too low n compared to the scaling-optimal ratio. When storage is limited, even an approximate choice of the lossy compression level can result in a significantly better trade-off between quality and quantity for computer vision tasks.

Acknowledgements

We are grateful to Joseph Gardi, Ayush Jain, Germain Kolossov, Marc Laugharn, Rahul Ponnala, Eren Sasoglu, and Pulkit Tandon for their feedback on this work. This work was carried out while Andrea Montanari was on leave from Stanford and a Chief Scientist at Granica (formerly known as Project N). The present research is unrelated to AM’s Stanford research.

References

- [Alabdulmohsin et al.(2022)] Ibrahim M Alabdulmohsin, Behnam Neyshabur, and Xiaohua Zhai. 2022. Revisiting neural scaling laws in language and vision. *Advances in Neural Information Processing Systems* 35 (2022), 22300–22312.
- [Alakuijala et al.(2019)] Jyrki Alakuijala, Ruud Van Asseldonk, Sami Boukourt, Martin Bruse, Iulia-Maria Comşa, Moritz Firsching, Thomas Fischbacher, Evgenii Kliuchnikov, Sebastian Gomez, Robert Obryk, et al. 2019. JPEG XL next-generation image compression architecture and coding tools. In *Applications of Digital Image Processing XLII*, Vol. 11137. SPIE, 112–124.
- [Bahri et al.(2021)] Yasaman Bahri, Ethan Dyer, Jared Kaplan, Jaehoon Lee, and Utkarsh Sharma. 2021. Explaining neural scaling laws. *arXiv preprint arXiv:2102.06701* (2021).
- [Bossard et al.(2014)] Lukas Bossard, Matthieu Guillaumin, and Luc Van Gool. 2014. Food-101 – Mining Discriminative Components with Random Forests. In *European Conference on Computer Vision*.
- [Cai et al.(2020)] Lei Cai, Jingyang Gao, and Di Zhao. 2020. A review of the application of deep learning in medical image classification and segmentation. *Annals of translational medicine* 8, 11 (2020).
- [Cheng and Montanari(2022)] Chen Cheng and Andrea Montanari. 2022. Dimension free ridge regression. *arXiv:2210.08571* (2022).
- [Cordts et al.(2016)] Marius Cordts, Mohamed Omran, Sebastian Ramos, Timo Rehfeld, Markus Enzweiler, Rodrigo Benenson, Uwe Franke, Stefan Roth, and Bernt Schiele. 2016. The Cityscapes Dataset for Semantic Urban Scene Understanding. In *Proc. of the IEEE Conference on Computer Vision and Pattern Recognition (CVPR)*.

- [Das et al.(2017)] Nilaksh Das, Madhuri Shanbhogue, Shang-Tse Chen, Fred Hohman, Li Chen, Michael E Kounavis, and Duen Horng Chau. 2017. Keeping the bad guys out: Protecting and vaccinating deep learning with jpeg compression. *arXiv preprint arXiv:1705.02900* (2017).
- [Daubechies(1992)] Ingrid Daubechies. 1992. *Ten lectures on wavelets*. SIAM.
- [Dodge and Karam(2016)] Samuel Dodge and Lina Karam. 2016. Understanding how image quality affects deep neural networks. In *2016 eighth international conference on quality of multimedia experience (QoMEX)*. IEEE, 1–6.
- [Donoho et al.(1998)] David L. Donoho, Martin Vetterli, Ronald A. DeVore, and Ingrid Daubechies. 1998. Data compression and harmonic analysis. *IEEE transactions on information theory* 44, 6 (1998), 2435–2476.
- [Dziugaite et al.(2016)] Gintare Karolina Dziugaite, Zoubin Ghahramani, and Daniel M Roy. 2016. A study of the effect of jpg compression on adversarial images. *arXiv preprint arXiv:1608.00853* (2016).
- [He et al.(2017)] Kaiming He, Georgia Gkioxari, Piotr Dollar, and Ross Girshick. 2017. Mask R-CNN. *2017 IEEE International Conference on Computer Vision (ICCV)* (Oct 2017).
- [He et al.(2016)] Kaiming He, Xiangyu Zhang, Shaoqing Ren, and Jian Sun. 2016. Deep residual learning for image recognition. In *Proceedings of the IEEE conference on computer vision and pattern recognition*. 770–778.
- [Henighan et al.(2020)] Tom Henighan, Jared Kaplan, Mor Katz, Mark Chen, Christopher Hesse, Jacob Jackson, Heewoo Jun, Tom B Brown, Prafulla Dhariwal, Scott Gray, et al. 2020. Scaling laws for autoregressive generative modeling. *arXiv preprint arXiv:2010.14701* (2020).
- [Hernandez et al.(2021)] Danny Hernandez, Jared Kaplan, Tom Henighan, and Sam McCandlish. 2021. Scaling laws for transfer. *arXiv preprint arXiv:2102.01293* (2021).
- [Hestness et al.(2017)] Joel Hestness, Sharan Narang, Newsha Ardalani, Gregory Diamos, Heewoo Jun, Hassan Kianinejad, Md Mostofa Ali Patwary, Yang Yang, and Yanqi Zhou. 2017. Deep learning scaling is predictable, empirically. *arXiv preprint arXiv:1712.00409* (2017).
- [Hoffmann et al.(2022)] Jordan Hoffmann, Sebastian Borgeaud, Arthur Mensch, Elena Buchatskaya, Trevor Cai, Eliza Rutherford, Diego de Las Casas, Lisa Anne Hendricks, Johannes Welbl, Aidan Clark, et al. 2022. Training compute-optimal large language models. *arXiv preprint arXiv:2203.15556* (2022).
- [JPEG([n. d.])] jpeg JPEG. [n. d.]. JPEG, An Overview of JPEG 1. <https://jpeg.org/jpeg/index.html>. Accessed: 2024-06-04.
- [Kaplan et al.(2020)] Jared Kaplan, Sam McCandlish, Tom Henighan, Tom B Brown, Benjamin Chess, Rewon Child, Scott Gray, Alec Radford, Jeffrey Wu, and Dario Amodei. 2020. Scaling laws for neural language models. *arXiv preprint arXiv:2001.08361* (2020).
- [Lin et al.(2014)] Tsung-Yi Lin, Michael Maire, Serge Belongie, James Hays, Pietro Perona, Deva Ramanan, Piotr Dollár, and C Lawrence Zitnick. 2014. Microsoft coco: Common objects in context. In *Computer Vision–ECCV 2014: 13th European Conference, Zurich, Switzerland, September 6–12, 2014, Proceedings, Part V 13*. Springer, 740–755.

- [Mallat(1999)] Stéphane Mallat. 1999. *A wavelet tour of signal processing*. Elsevier.
- [Muennighoff et al.(2023)] Niklas Muennighoff, Alexander M Rush, Boaz Barak, Teven Le Scao, Aleksandra Piktus, Nouamane Tazi, Sampo Pyysalo, Thomas Wolf, and Colin Raffel. 2023. Scaling Data-Constrained Language Models. *arXiv preprint arXiv:2305.16264* (2023).
- [Roelofs([n. d.])png Greg Roelofs. [n. d.]. PNG, Portable Network Graphics. <http://libpng.org/pub/png/>. Accessed: 2024-06-04.
- [Rombach et al.(2022)] Robin Rombach, Andreas Blattmann, Dominik Lorenz, Patrick Esser, and Björn Ommer. 2022. High-resolution image synthesis with latent diffusion models. In *Proceedings of the IEEE/CVF conference on computer vision and pattern recognition*. 10684–10695.
- [Rosenfeld et al.(2019)] Jonathan S Rosenfeld, Amir Rosenfeld, Yonatan Belinkov, and Nir Shavit. 2019. A Constructive Prediction of the Generalization Error Across Scales. In *International Conference on Learning Representations*.
- [Schuhmann et al.(2022)] Christoph Schuhmann, Romain Beaumont, Richard Vencu, Cade Gordon, Ross Wightman, Mehdi Cherti, Theo Coombes, Aarush Katta, Clayton Mullis, Mitchell Wortsman, et al. 2022. Laion-5b: An open large-scale dataset for training next generation image-text models. *Advances in Neural Information Processing Systems* 35 (2022), 25278–25294.
- [Tay et al.(2021)] Yi Tay, Mostafa Dehghani, Jinfeng Rao, William Fedus, Samira Abnar, Hyung Won Chung, Sharan Narang, Dani Yogatama, Ashish Vaswani, and Donald Metzler. 2021. Scale Efficiently: Insights from Pretraining and Finetuning Transformers. In *International Conference on Learning Representations*.
- [Theis et al.(2022)] Lucas Theis, Wenzhe Shi, Andrew Cunningham, and Ferenc Huszár. 2022. Lossy image compression with compressive autoencoders. In *International conference on learning representations*.
- [Tsigler and Bartlett(2023)] Alexander Tsigler and Peter L Bartlett. 2023. Benign overfitting in ridge regression. *Journal of Machine Learning Research* 24, 123 (2023), 1–76.
- [Vryniotis(2021)] Vasilis Vryniotis. 2021. How to Train State-Of-The-Art Models Using TorchVision’s Latest Primitives. <https://pytorch.org/blog/how-to-train-state-of-the-art-models-using-torchvision-latest-primitives/>. Accessed: 2024-01-29.
- [Waqas Zamir et al.(2019)] Syed Waqas Zamir, Aditya Arora, Akshita Gupta, Salman Khan, Guolei Sun, Fahad Shahbaz Khan, Fan Zhu, Ling Shao, Gui-Song Xia, and Xiang Bai. 2019. iSAID: A Large-scale Dataset for Instance Segmentation in Aerial Images. In *Proceedings of the IEEE Conference on Computer Vision and Pattern Recognition Workshops*. 28–37.
- [Xie et al.(2021)] Enze Xie, Wenhai Wang, Zhiding Yu, Anima Anandkumar, Jose M. Alvarez, and Ping Luo. 2021. SegFormer: Simple and Efficient Design for Semantic Segmentation with Transformers. *CoRR* abs/2105.15203 (2021). arXiv:2105.15203 <https://arxiv.org/abs/2105.15203>
- [Yang et al.(2021)] En-Hui Yang, Hossam Amer, and Yanbing Jiang. 2021. Compression helps deep learning in image classification. *Entropy* 23, 7 (2021), 881.

A Training Details

A.1 Image Classification

For the classification task, we take subsets of the data of size $n \in \{12120, 24240, 36360, 48480, 60600\}$, stratified by training labels, to generate different values of n . For each pair (n, L) , we train 5 different models with different random seeds, and the reported performance is the average performance across the 5 models. Each model is trained using cross entropy loss for 10 epochs with a batch size of 64 and a learning rate of 0.0001.

A.2 Semantic Segmentation

In the segmentation task, we use sample sizes $n \in \{595, 1190, 1785, 2380, 2975\}$. Each model was trained using cross entropy loss for 80,000 steps with a batch size of 3. The learning rate has a linear warm up over the first 1,500 steps, reaching a maximum of 6×10^{-6} , then decreasing linearly for the remainder of the steps.

A.3 Object Detection

For the iSAID dataset, we consider $n \in \{5605, 11211, 16817, 22423, 28029\}$. We train each object detection model for 12 epochs. The learning rate begins with a warm up phase, starting 2×10^{-5} and increasing to 0.02 over the course of 500 iterations. Then, a multi-step learning rate schedule is used, multiplying the learning rate by a factor of 0.1 after the 8th and 11th epochs. Each point is averaged over two iterations from two different random seeds.

B Scaling Curves in Additional Metrics

Figure 7 illustrates scaling curves with alternative error metrics. Figure 7a-b show the multi-class F1 score scaling curve for the classification task. Figure 7c-d shows the mean accuracy scaling curve for the segmentation task. The architecture used for the object detection task, a Mask R-CNN, can also provide instance segmentation predictions, and Figure 7e-f shows the mean average precision test error for these segmentation predictions. The results suggest that scaling shows a similar pattern regardless of the specific metric used to evaluate model performance.

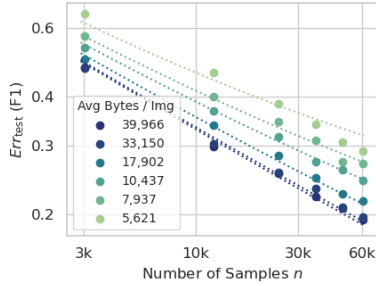
C Omitted proofs

In this appendix we prove the statements of Section 3. We begin by formally stating our assumption about the feature vectors \mathbf{x}_i .

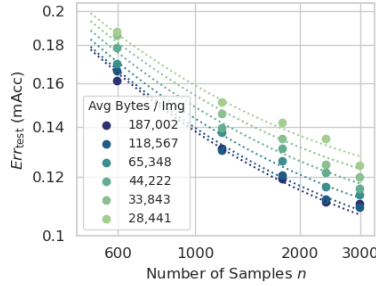
Assumption 1. *Let $\mathbf{x} = (\mathbf{x}^{(0)}, \mathbf{x}^{(1)}, \mathbf{x}^{(2)}, \dots)$ be distributed as any of the feature vectors \mathbf{x}_i and define $\mathbf{z}^{(\ell)} = \mathbf{x}^{(\ell)} / \sqrt{s_\ell}$. In particular $\mathbb{E}\mathbf{z}^{(\ell)} = \mathbf{0}$ and $\mathbb{E}\{\mathbf{z}^{(\ell)}(\mathbf{z}^{(\ell)})^\top\} = \mathbf{I}_{q^\ell}$. We assume either one of the following to hold:*

- (a) *For each ℓ , the entries of $\mathbf{z}^{(\ell)}$ are independent sub-Gaussian.*
- (b) *For each ℓ , $\mathbf{z}^{(\ell)}$ satisfies a log-Sobolev inequality with ℓ -independent constant C .*
- (c) *For each ℓ , $\mathbf{z}^{(\ell)}$ satisfies the following concentration property, with ℓ -independent constant C . For any convex 1-Lipschitz function φ and any t ,*

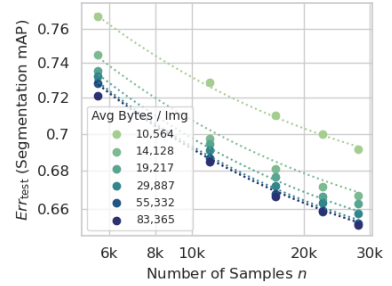
$$\mathbb{P}(\varphi(\mathbf{z}^{(\ell)}) - \mathbb{E}\varphi(\mathbf{z}^{(\ell)}) \geq t) \leq e^{-t^2/2C}. \quad (23)$$



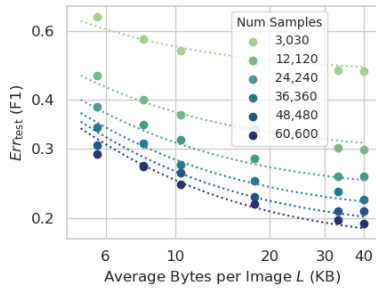
(a) Classification F1 scaling in n



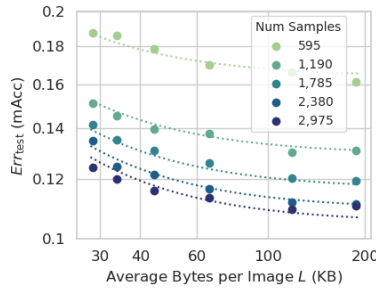
(c) Segmentation mean accuracy scaling in n



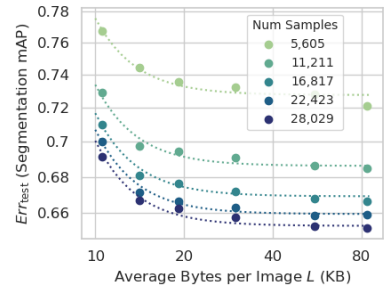
(e) Mask R-CNN segmentation mean average precision scaling in n



(b) Classification F1 scaling in L



(d) Segmentation mean accuracy scaling in L



(f) Mask R-CNN segmentation mean average precision scaling in L

Figure 7: Scaling patterns for alternative metrics for each task. For the image classification task, we show multi-class F1 score as the error metric, for the semantic segmentation task, we use mean accuracy, and for the object detection task, we use the mean average precision for all objects from the Mask R-CNN’s segmentation predictions.

We note in passing that condition (b) above is a special case of (c) and we state it for the sake of readability.

Throughout, we write $F(n) \asymp G(n)$ if there exist constants $0 < C_1 < C_2$ such that $C_1 \cdot G(n) \leq F(n) \leq C_2 \cdot G(n)$. We also use C, C_1, \dots for generic constants that can change from line to line. Throughout the proof, we assume $n \leq cL$. The case $cL \leq n \leq c_*L^{1+2\kappa}$ is treated analogously.

C.1 Evaluation of $B(m, n)$, $V(m, n)$, λ_*

We begin by evaluating the quantities appearing in Lemma 1. Begin by Eq. (15), which we rewrite as

$$n = \frac{\lambda}{\lambda_*} + F(\lambda_*). \quad (24)$$

Letting ℓ_* be such that $p^{-\ell_*-1} \leq \lambda_* < p^{-\ell_*}$, we have

$$\begin{aligned} F(\lambda_*) &= \sum_{\ell \leq \ell_*} \frac{(q/p)^\ell}{p^{-\ell} + \lambda_*} + \sum_{\ell=\ell_*+1}^m \frac{(q/p)^\ell}{p^{-\ell} + \lambda_*} \\ &= \sum_{\ell \leq \ell_*} \frac{(q/p)^\ell}{p^{-\ell}} + \sum_{\ell=\ell_*+1}^m \frac{(q/p)^\ell}{p^{-\ell_*}} \\ &\asymp q^{\ell_* \wedge m} \asymp \lambda_*^{-1/\kappa} \wedge q^m. \end{aligned}$$

Therefore, Eq. (24) reduces to

$$\frac{\lambda}{\lambda_*} + C_1 \lambda_*^{-1/\kappa} \wedge q^m \leq n \leq \frac{\lambda}{\lambda_*} + C_2 \lambda_*^{-1/\kappa} \wedge q^m. \quad (25)$$

We therefore distinguish two cases (with c_0 a small constant):

$$n \leq c_0 q^m \Rightarrow \lambda_* \asymp \frac{\lambda}{n} \vee n^{-\kappa}, \quad (26)$$

$$n > c_0 q^m \Rightarrow \lambda_* \asymp \frac{\lambda}{n}. \quad (27)$$

Pursuing the first case, we have

$$\begin{aligned} D(m) &\asymp \sum_{\ell=0}^m \frac{q^\ell p^{-2\ell}}{(\lambda_* + p^{-\ell})^2} \\ &\asymp \sum_{\ell=0}^{\ell_*} q^\ell + \sum_{\ell=\ell_*+1}^m q^\ell p^{-2(\ell-\ell_*)} \\ &\asymp q^{\ell_* \wedge m}. \end{aligned}$$

Further, by comparing the terms $\ell = \ell_*$ of $D(m)$ and $F(\lambda_*)$ we obtain that $D(m) \leq (1 - c_1)F(\lambda_*)$ for some positive constant c_1 .

Substituting in the formula for V , we get

$$V(m, n) \asymp \frac{1}{n} q^{\ell_* \wedge m} \asymp (\lambda^{-1/\kappa} n^{-1+1/\kappa} \wedge 1). \quad (28)$$

We further have (using $rp < 1$)

$$\begin{aligned} \sum_{\ell=0}^m \frac{s_\ell \|\boldsymbol{\theta}^{(\ell)}\|^2}{(s_\ell + \lambda_*)^2} &\asymp \sum_{\ell=0}^m \frac{r^\ell p^{-\ell}}{(p^{-\ell} + \lambda_*)^2} \\ &\asymp \sum_{\ell=0}^{\ell_*} \frac{r^\ell}{p^{-\ell}} + \sum_{\ell=\ell_*+1}^m \frac{r^\ell p^{-\ell}}{p^{-2\ell_*}} \\ &\asymp 1, \end{aligned}$$

whence

$$\mathbf{B}(m, n) \asymp \lambda_*^2 \asymp \left(\frac{\lambda}{n}\right)^2 \vee n^{-2\kappa}.$$

C.2 Proof of Lemma 1

This lemma is an application of Proposition 4.3 in [Cheng and Montanari(2022)]. We only need to check the assumptions of that proposition, and compute error terms, which we do below (following notations from [Cheng and Montanari(2022)], end denoting by $b_\ell := (1 - q^\ell)/(1 - q)$):

1. *Effective dimension* \mathbf{d}_Σ . Note that, for $k \in [b_\ell + 1, b_{\ell+1}]$, we have

$$\sum_{i \geq k} \sigma_i \leq C \sum_{j \geq \ell} p^{-j} q^j \leq C q^\ell \sigma_k. \quad (29)$$

and for $k \leq n$, the last expression is at most $Cn\sigma_k$. Therefore $\mathbf{d}_\Sigma \asymp n$.

2. *Effective regularization* $\lambda_*(\lambda)$. This quantity is analyzed in the previous section, implying that for $n \leq c_0 L$, $\lambda_*(\lambda) \asymp (n^{-\kappa} \wedge (\lambda/n))$. In particular, $\lambda \in [n\lambda_*(\lambda)/M, n\lambda_*(\lambda)M]$ under the assumptions of the lemma. (Note that Proposition 4.3 in [Cheng and Montanari(2022)] states this condition as $\lambda \in [n\lambda_*(0)/M, n\lambda_*(0)M]$, but the condition checked here is also sufficient.)
3. *Coefficient* $\rho(\lambda)$. Recalling the general definition from [Cheng and Montanari(2022)], we have:

$$\rho(\lambda) = \frac{\sum_{\ell=0}^m \|\boldsymbol{\theta}^{(\ell)}\|^2 / (s_\ell + \lambda_*)}{F(\lambda_*) \sum_{\ell=0}^m \|\boldsymbol{\theta}^{(\ell)}\|^2 / s_\ell}, \quad (30)$$

where λ_* is determined by Eq. (15) (we note in passing a difference in notation with respect to [Cheng and Montanari(2022)], since we use $\boldsymbol{\theta}$ for what is denoted by $\boldsymbol{\beta}$ there.)

Various terms are estimated analogously to the last section. First consider the denominator

$$\begin{aligned} F(\lambda_*) &\asymp \lambda_*^{-1/\kappa} \asymp \left(\frac{\lambda}{n}\right)^{-1/\kappa} \wedge n, \\ \sum_{\ell=0}^m \|\boldsymbol{\theta}^{(\ell)}\|^2 / s_\ell &\asymp \sum_{\ell=0}^m (rp)^\ell \asymp 1. \end{aligned}$$

Considering next the numerator:

$$\begin{aligned} \sum_{\ell=0}^m \frac{\|\boldsymbol{\theta}^{(\ell)}\|^2}{s_\ell + \lambda_*} &\asymp \sum_{\ell=0}^m \frac{r^\ell}{p^{-\ell} + \lambda_*} \\ &\asymp \sum_{\ell=0}^{\ell_*} \frac{r^\ell}{p^{-\ell}} + \sum_{\ell=\ell_*+1}^m \frac{r^\ell}{p^{-\ell_*}} \asymp 1 \end{aligned}$$

Putting everything together, we obtained

$$\rho(\lambda) = \left(\frac{\lambda}{n}\right)^{1/\kappa} \vee \frac{1}{n}. \quad (31)$$

We finally applying Proposition 4.3 in [Cheng and Montanari(2022)]. to the second term of (13), which reduces to the setting of [Cheng and Montanari(2022)] with τ^2 replaced by $\tilde{\tau}_m^2$. We obtain that, for $\lambda \in [n^{-\kappa}/M, n^{-\kappa}M]$, with M an arbitrary constant, and dropping the arguments from $\mathcal{B}, \mathcal{V}, \mathbf{B}, \mathbf{V}$,

$$|\mathcal{V} - \mathbf{V}| \leq O(n^{-1+\varepsilon}) \cdot \mathbf{V}, \quad (32)$$

$$|\mathcal{B} - \mathbf{B}| \leq O(\rho(\lambda)^{-1/2} n^{-1+\varepsilon}) \cdot \mathbf{B} = O(n^{-1/2+\varepsilon}) \cdot \mathbf{B}, \quad (33)$$

which proves our claim.

C.3 Proof of Theorem 1

Collecting the expressions for bias and variance from Section C.1

$$\begin{aligned} K_V(\lambda^{-1/\kappa} n^{-1+1/\kappa} \wedge 1) \leq \mathbf{V}(m, n) \leq K'_V(\lambda^{-1/\kappa} n^{-1+1/\kappa} \wedge 1), \\ K_B \left[\left(\frac{\lambda}{n}\right)^2 \vee n^{-2\kappa} \right] \leq \mathbf{B}(m, n) \leq K'_B \left[\left(\frac{\lambda}{n}\right)^2 \vee n^{-2\kappa} \right]. \end{aligned}$$

Using the choice $\lambda \asymp n^{(\kappa+1)/(2\kappa+1)}$ as in the statement on the theorem, we get (eventually adjusting the constants):

$$\begin{aligned} K_V n^{-\alpha} \leq \mathbf{V}(m, n) \leq K'_V n^{-\alpha}, \\ K_B n^{-\alpha} \leq \mathbf{B}(m, n) \leq K'_B n^{-\alpha}. \end{aligned}$$

Substituting in Lemma 1, we get

$$\mathbb{E}_\varepsilon \mathbf{Err}_{\text{test}}(n, L) \leq \tau^2 + A \cdot n^{-\alpha} + B \cdot (r/p)^m.$$

The upper bound in the theorem follows by recalling the relation between m and L . The lower bound follows by modifying the last two steps.